*J. Electrochem. Sci. Eng.* **15(3)** (2025) 2655; http://dx.doi.org/10.5599/jese.2655

Open Access : : ISSN 1847-9286
www.jESE-online.org

*Original scientific paper*

# Correlation between diffusion and kinetic behaviour of metal hydride battery: voltammetry and impedance analyses

Ika Dewi Wijayanti✉, Delia Salsabila Sri Putri, Farhan Dzikriansyah, Indra Sidharta and Sutikno Sutikno

*Department of Mechanical Engineering, ITS, Surabaya,60111, Indonesia*

*Corresponding author: ✉ika.dewi.wijayanti@its.ac.id; Tel.: +62-31-5994251-54; Fax: +62-31-5923465*

Received: January 24, 2025; Accepted: March 13, 2025; Published: April 14, 2025

***Abstract***

*The performance of metal hydride batteries depends on their electrochemical and kinetic behaviour, which varies with the state of charge (SoC). This study explores these characteristics in nickel-metal hydride batteries with $A_2B_7$ and $AB_5$ electrodes, focusing on how SoC influences ion diffusion and charge transfer kinetics of the batteries. Electrochemical impedance spectroscopy and cyclic voltammetry (CV) were used to analyse these behaviours, while X-ray diffraction provided structural insights and scanning electron microscopy proposed morphological concepts. Results reveal a positive correlation between SoC and both diffusion and kinetic behaviour. The value of fitting resistances decreases as SoC increases, reaching a minimum at 100 % SoC, where hydrogen diffusion is optimized. CV data supports this phenomenon, showing a more negative peak cathodic current ($I_{p,c}$) at higher SoC, indicating improved kinetics likely due to enhanced ion availability. Additionally, voltage window analysis showed maximum hydrogen storage at 100 % SoC for $AB_5$ and 50 % for $A_2B_7$. Structurally, larger particle sizes and crystallites at higher SoC correlate with increased hydrogen desorption capacity. $A_2B_7$ exhibited superior diffusion kinetics, while $AB_5$ demonstrated better discharge behaviour, highlighting how SoC-dependent diffusion and kinetics impact Ni-MH performance.*

**Keywords**

State of charge; hydrogen storage alloys; performance analysis; Nyquist plots; voltage window

## Introduction

A battery is an energy storage device that facilitates effective energy storage and management, particularly for applications with intermittent energy supply [1,2]. Energy storage in batteries occurs through the conversion of chemical energy into electrical energy within individual cells via redox (reduction-oxidation) reactions [3,4]. Batteries are broadly classified by their rechargeability into two categories: primary (non-rechargeable) and secondary (rechargeable) types [5,6]. One of the secondary battery types is the Ni-MH battery [7].

Ni-MH battery is an energy storage system that operates through electrochemical charge and discharge reactions between its positive and negative electrodes: nickel hydroxide $Ni(OH)_2$ and hydrogen-absorbing alloys. Studying Ni-MH batteries is increasingly important due to their widespread use in various applications, including electric vehicles, consumer electronics, and renewable energy storage systems. Their relatively high energy density, safety profile, and environmental compatibility make them a valuable alternative to other battery types, such as nickel-cadmium and even lithium-ion batteries, in certain applications. According to Technavio, the global Ni-MH battery market grew at a compound annual growth rate (CAGR) of 2.63 % from 2018 to 2022, with projected growth set to reach 3.1 % from 2023 to 2028, reflecting a steady increase in demand. This growth underscores the need for ongoing research to optimize Ni-MH battery performance, lifespan, and sustainability [8,9].

Despite their promise as an alternative to lithium-ion batteries, Ni-MH batteries remain less widely studied, particularly concerning the impact of diffusion and kinetic behaviours on performance [10-12]. The interplay between ion diffusion and reaction kinetics is critical to the overall efficiency, charge capacity, and cycle life of Ni-MH batteries, as these factors determine how well the battery maintains energy transfer and conversion at different states of charge SoC [13-15]. A detailed understanding of this correlation is essential to optimize Ni-MH battery design, enhance hydrogen diffusion rates, and minimize resistance, directly influencing the battery's ability to store and release energy efficiently [16-18].

Battery performance is also highly influenced by user behaviour, including charging habits and usage patterns, particularly the maintained SoC [19,20]. SoC affects the electrochemical balance of battery electrodes, with variations leading to differences in capacity retention, cycle life, and even resistance and Warburg coefficient values, which reflect impedance and hydrogen diffusion properties [21,22]. Resistance impacts the current flow within electrode and electrolyte materials, while the Warburg coefficient value relates to hydrogen ion mobility within the cell, which is essential for optimal efficiency and capacity [23,24].

This study presents a novel and comprehensive approach to understanding Ni-MH battery performance by uniquely correlating diffusion and kinetic behaviours with SoC variations, a factor often overlooked in previous research. Unlike prior studies that primarily focus on either electrochemical performance or structural characterization in isolation, this work integrates CV and EIS to simultaneously analyse ion-transfer kinetics and hydrogen diffusion rates across varying SoC levels. Furthermore, XRD and SEM analyses provide unprecedented insights into how crystal structure and electrode surface morphology evolve with SoC, directly linking structural transformations to electrochemical behaviour.

The novelty of this study lies in its ability to establish a direct correlation between SoC, diffusion coefficients, charge transfer resistance, and morphological changes, which have not been comprehensively explored before. The findings reveal critical SoC thresholds that optimize hydrogen diffusion while minimizing resistance, offering practical guidance for battery operation and design improvements. By bridging the gap between electrochemical kinetics and material science, this research advances the understanding of Ni-MH batteries beyond conventional studies and enhances their potential as high-performance, energy-efficient storage solutions.

## Experimental

### *Materials*

In this study, AA-type Ni-MH batteries with a rated capacity of 1900 mAh were selected as the research materials. Two commercially common metal hydride types, $AB_5$ and $A_2B_7$, were chosen for analysis. X-ray diffraction (XRD) was used to confirm the metal hydride phase structure of the batteries, identifying $Ce(CoCu)_{2.5}$ in the $AB_5$ type and $Ce_2Ni_7$ in the $A_2B_7$ type. To investigate the effects of SoC on battery behaviour, individual battery samples were set at SoC levels of 0, 20, 50, 80 and 100 %. All charging and testing procedures were conducted at room temperature.

### *Actual capacity and SoC measurement*

Prior to charging the batteries to achieve different SoC levels, actual capacity measurements were performed on each battery. Starting from an empty state, the batteries were charged at a constant current of 100 mA (0.053C) until reaching a total charge of 2000 mAh, indicating full charge. They were then discharged at a low current of 10 mA until a cutoff voltage of 0.7 V, indicating full discharge. The actual capacity was defined as the total capacity discharged from a fully charged to a fully discharged state. With the actual capacity determined, the batteries were charged to the target SoC levels. All capacity measurements and charging processes were conducted using a Landt Instruments CT3002A battery tester.

### *Cyclic voltammetry testing*

CV testing was conducted using a Potentiostat PGSTAT302N within 24 hours of charging. The scan began at an initial potential of 0 V and proceeded to a switching potential of 2 V, with a scan rate of 0.5 mV $s^{-1}$. Each battery sample underwent a total of three cycles. The testing utilized a full-cell, two-electrode configuration, observing both the negative and positive electrodes of the battery [25].

### *Electrochemical impedance spectroscopy testing*

Electrochemical impedance spectroscopy (EIS) testing for each battery was conducted at the open circuit voltage (OCV) under identical conditions, covering a frequency range from 5000 to 0.01 Hz with 10 data points per frequency decade and an amplitude of 0.01 V. The objective of this testing was to assess resistance and Warburg coefficient values for each battery sample. Data fitting was performed using Zview software [26] to analyse values derived from the Nyquist plots, employing the electrical equivalent circuit depicted in Figure 1. Within this circuit, $R_1$ corresponds to the electrolyte, including separator resistance, $R_2$ indicates the contact resistance between the alloy particles and the current collector, and $R_3$ pertains to the charge transfer resistance. The constant phase elements ($CPE_1$ and $CPE_2$) represent the capacitive impedance characteristics, modelling the behaviour of an imperfect capacitor at the electrode, while Warburg impedance ($W$) accounts for mass transport limitations associated with hydrogen ion diffusion [27].


***Figure 1.*** *Electrical equivalent circuit for fitting process of Nyquist plots [28]*

## Results and discussion

### *Actual capacity*

The actual capacity of the batteries made with $AB_5$ and $A_2B_7$ materials from an SoC of 0 to 100 % is illustrated in Figure 2. Both batteries exhibit similar capacities across all SoC levels, except at 80

and 100 % SoC, where notable differences are observed. This indicates that both material types show comparable performance. It is evident that across all SoC levels, the battery capacities are nearly identical, except at 80 and 100 % SoC. At these points, the $AB_5$ battery demonstrates a higher capacity, suggesting that the $AB_5$ material may achieve a more complete activation at higher states of charge [29].

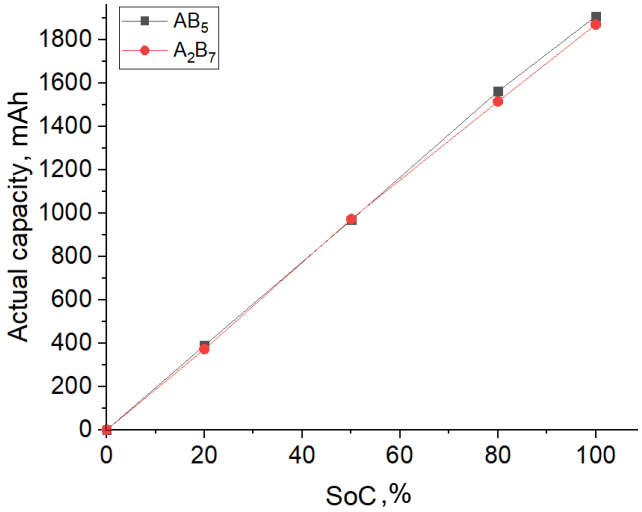


***Figure 2.*** *Actual capacity of the batteries with $AB_5$ and $A_2B_7$ types of metal hydrides*

*Nyquist plots*

Figure 3 illustrates the Nyquist plots for both batteries across a SoC range of 0 to 100 %. The graph presents both experimental and fitted plots, initially showing a pronounced difference between the two, which decreases as the SoC rises. This reduction in the goodness of fit at higher SoC levels indicates that the proposed fitted values exhibit smaller differences and narrower distributions. Consequently, at higher SoC, the resistance values become easier to approximate, increasing the likelihood of alignment between the experimental data and the proposed values [30]. This phenomenon is illustrated in Figure 3(e). The battery using the $A_2B_7$ material demonstrates a lower goodness of fit compared to the $AB_5$ material, indicating that the electrochemical resistances are more accurately represented, particularly at higher SoC levels. The resulting chi-square values confirm that the model effectively captures the electrochemical processes and accurately represents the entire SoC range during charge and discharge cycles.

Moreover, the Nyquist plots of both batteries exhibit imperfect semicircle shapes indicating the presence of non-ideal capacitive behaviour in an electrochemical system [31]. A reduction in the semicircular shape of the Nyquist plot with increasing SoC indicates that electron movement and mass transport become more restricted at lower charge levels (Figures 3(a) and 3(b)). At higher SoC, the battery electrodes are likely to exhibit improved ion and electron transport, attributed to more uniform charge distribution and increased surface activation of the electrodes. These conditions contribute to reduced charge transfer and diffusion resistances, facilitating electrochemical reactions. Furthermore, the elevated electrode potential at higher SoC increases the concentration of ions near the electrode surface. This effect aligns with the Gouy-Chapman model, wherein the diffuse ion layer becomes more compact, leading to an enhanced double-layer capacitance [32-34].

The Nyquist plot provides a comprehensive representation of the real and imaginary components of impedance, offering valuable insights into the electrochemical and charge transfer mechanisms within battery systems. The real impedance reflects the resistance in the electrical circuit, while the imaginary impedance, influenced by inductance and capacitance, captures the dynamic electro

-chemical processes and charge transfer mechanisms occurring between the electrodes. These behaviours are often attributed to differences in surface structure and ion mobility of the electrode materials [35].

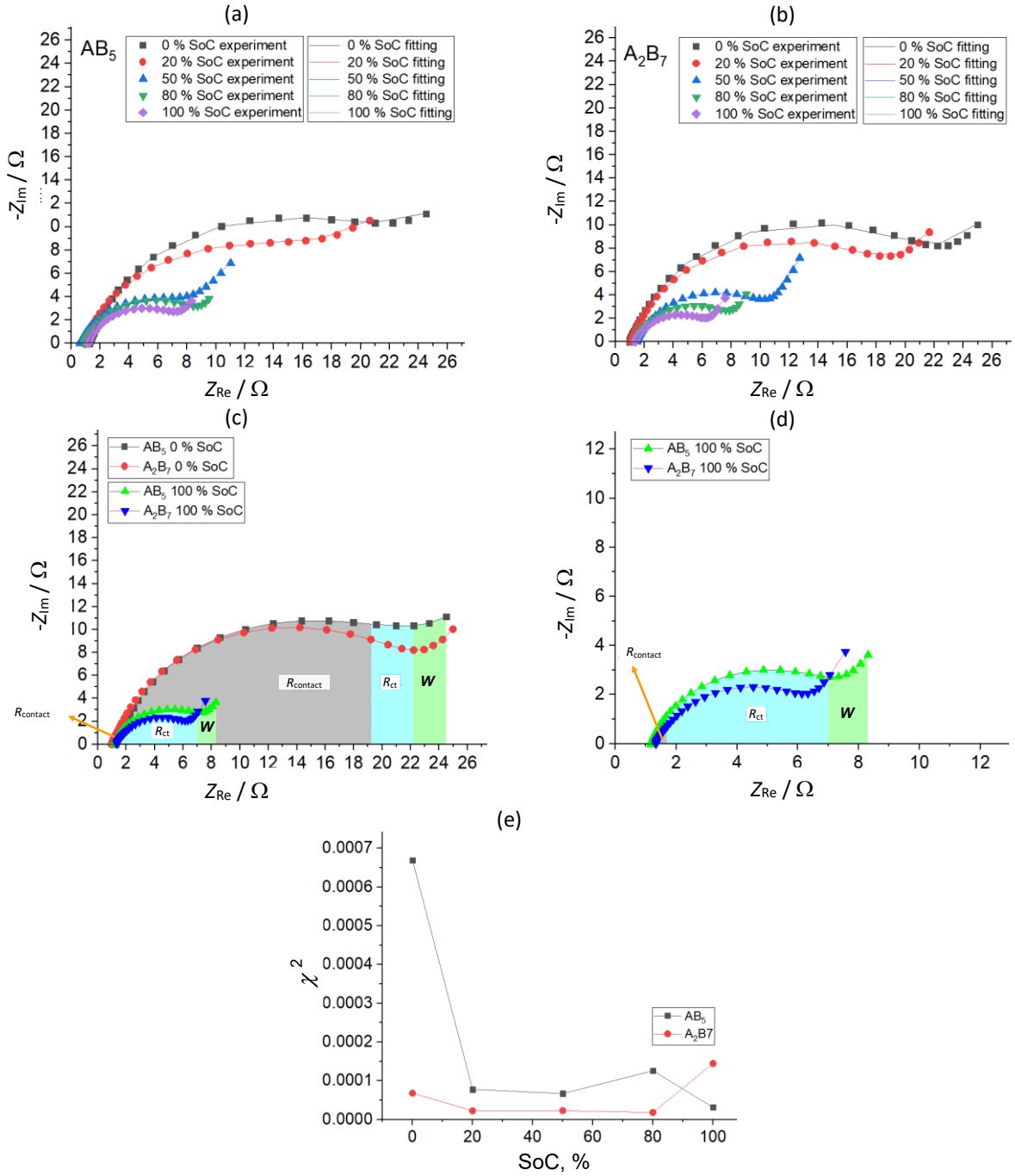


***Figure 3***. *The Nyquist plots of the batteries with $AB_5$ (a) and $A_2B_7$ (b) materials, fitted with the equivalent circuit for fitting shown in Fig. 1. The distinct shapes of the Nyquist plots for the two batteries at 100 and 0 % SoC highlight significant differences in their electrochemical behaviour (c). Additionally, the Nyquist plot of both batteries at 100 % SoC is displayed on a smaller scale for clarity (d). The colors in the graphs represent the approximate values of fitting resistance: grey indicates contact resistance between alloy particles and the current collector, green represents charge transfer resistance, and blue corresponds to Warburg impedance. The lower goodness of fit plots for both batteries show the high conformity between the equivalent circuit model with the proposed resistance, capacitance, and Warburg impedance values (e)*

A comparative analysis of Nyquist plots for $AB_5$ and $A_2B_7$ materials at identical SoC levels reveals distinct impedance characteristics. At higher SoC levels, the $AB_5$ material exhibits a greater

imaginary impedance in the low-frequency region, indicating a more pronounced capacitive or inductive response within the system, which is influenced by charge transfer, ion diffusion, and electrode surface characteristics, whereas the $A_2B_7$ material demonstrates a lower imaginary impedance. The $AB_5$ material exhibits a higher energy storage capacity or slower charge transfer dynamics compared to the $A_2B_7$ material. At lower SoC levels, both materials display similar impedance characteristics, with real and imaginary components decreasing across frequencies. However, as the frequency increases, the $AB_5$ material shows a more pronounced rise in imaginary impedance compared to $A_2B_7$, highlighting essential differences in their electrochemical performance. The higher imaginary impedance of $AB_5$ at low frequencies suggests greater energy storage capability but potential diffusion limitations, whereas the lower imaginary impedance of $A_2B_7$ indicates more efficient ion transport and faster charge transfer reactions due to a less resistive interface [36]. These differences are critical in determining the optimal operating conditions and overall efficiency of metal hydride batteries, influencing their charge/discharge rates and cycle life. These observed phenomena can be attributed to the underlying capacitance and inductance effects in the Nyquist plots. Capacitance, primarily originating from the double-layer capacitance at the electrode/electrolyte interface, represents the system's ability to store charge. The $AB_5$ material's larger imaginary impedance may indicate a contribution of higher double-layer capacitance, suggesting a more developed interfacial area conducive to charge accumulation but with increased charge transfer resistance. Inductance, although less commonly observed, also plays a role in the dynamic behaviour of the system. Inductive contributions, visible as positive imaginary impedance, can arise from adsorption/desorption on the electrode surface or non-idealities in the experimental setup. The more significant imaginary impedance observed in the $AB_5$ material at lower frequencies may reflect delayed system responses due to slower adsorption/desorption kinetics or greater structural heterogeneity. These inductive and capacitive behaviours collectively shape the distinct impedance characteristics of the $AB_5$ and $A_2B_7$ materials, highlighting their differing electrochemical properties and underlying charge transfer mechanisms [37].

The SoC variation significantly influences the impedance components of $AB_5$ and $A_2B_7$ battery materials, as illustrated by the detailed analysis in Figures 3(c) and (d). At 100 % SoC, the $AB_5$ battery exhibits distinctive electrochemical characteristics: a notable reduction in contact resistance, accompanied by an increased charge transfer resistance and a diminished Warburg impedance. Conversely, the $A_2B_7$ battery demonstrates a different electrochemical profile, characterized by reduced charge transfer resistance and an expanded Warburg impedance compared to the $AB_5$ battery. In this case, the $AB_5$ material reveals a pronounced oxidation tendency and enhanced corrosion susceptibility, which manifest prominently in the high-frequency impedance spectrum. In contrast, the $A_2B_7$ material displays distinctive behaviour, with notable pulverization and reduced oxidation, evidenced by the decreased charge transfer resistance and concurrent increase in Warburg impedance, predominantly observed in the low-frequency region. The more extensive pulverization of the $A_2B_7$ material initiates the micro-cracking of metal hydride alloy powders, resulting in the fragmentation into smaller particles. This structural transformation significantly increases the electrode's real surface area, consequently enhancing the kinetic properties of electrode reactions. These observations elucidate the fundamental electrochemical and structural disparities between $AB_5$ and $A_2B_7$ materials [38,39]. To summarize, at 0 % SoC: the impedance spectra show that the contact resistance ($R_2$) dominates over the charge transfer resistance ($R_3$). This can be attributed to the limited availability of charge carriers at a fully discharged state, resulting in higher interfacial resistance. Additionally, surface effects such as SEI layer formation may contribute to an increased contact resistance. At 100 % SoC,

the contact resistance ($R_2$) decreases due to improved electronic conduction within the electrode as charge carriers become more available. Conversely, the charge transfer resistance ($R'$) increases, likely due to the lower electrochemical reaction kinetics at a fully charged state, where ion transport limitations may become more significant. These trends are consistent with prior electrochemical impedance studies [28] and align with the expected behaviour of electrode materials under different SOC conditions.

In this study, the selection of the electrical equivalent circuit (EEC) model, comprising two RC elements and a Warburg impedance ($W$), was based on the necessity to account for distinct electrochemical processes occurring within the system. The first RC combination ($R_2$/$CPE_1$) represents the contact resistance at the electrode/electrolyte interface and the capacitive behaviour of interfacial layers, while the second RC combination ($R_3$/$CPE_2$) corresponds to the charge transfer resistance and double-layer capacitance at the active electrode surface. The Warburg element ($W$) accounts for the semi-infinite diffusion of ions in the electrolyte. A model with only one RC element ($C_{dl}$/$R_{ct}$) and Warburg impedance would not sufficiently describe the observed impedance behaviour at different states of charge (SoC). Previous studies [28,40,41] have also employed a two-RC model to distinguish interfacial and charge transfer contributions in similar electrochemical systems.

To validate the model, we performed a fitting analysis with different EEC configurations and found that the two RC models yielded the lowest fitting error and best agreement with the experimental data. Nyquist plot fitting (Figure 3) was conducted using a modified Randles circuit incorporating constant phase elements (CPE) to compensate for surface inhomogeneities (Figure 1) and was processed with ZView software. The extracted impedance parameters include electrolyte involving separator resistance ($R_1$), contact resistance between alloy particles and the current collector ($R_2$), charge transfer resistance ($R_3$), and Warburg impedance ($W$). The fitted parameter values are presented in Figure 4.

For the $AB_5$ battery, electrolyte resistance ($R_1$) exhibits notable variation, decreasing at mid-range SoC and increasing at full SoC, suggesting ion mobility through the electrolyte is optimal at intermediate SoC levels. As the SoC increases, the charge transfer resistance ($R_3$) significantly decreases, indicating enhanced charge transfer kinetics, which improves the alloy's electrocatalytic activity and retention rate [42]. The contact resistance between alloy particles and the current collector ($R_2$) is lowest at mid-range SoC and peaks at full SoC, reflecting changes in the electrode surface structure and ion interactions. Warburg impedance, representing hydrogen ion diffusion, decreases at higher SoC, indicating more efficient diffusion processes.

A similar trend is observed for the $A_2B_7$ battery, where $R_1$ decreases with increasing SoC, reaching its lowest value at full SoC. The charge transfer resistance ($R_3$) also declines, confirming improved electrochemical kinetics at higher SoC. However, the contact resistance ($R_2$) follows a different pattern, exhibiting higher values at low and full SoC, with the lowest resistance at intermediate SoC. Warburg impedance progressively decreases with increasing SoC, indicating enhanced hydrogen diffusion capabilities at higher SoC levels.

To ensure the reliability of the extracted parameters, Table 1 summarizes all six impedance parameters along with their respective errors. The fitting error was assessed using the chi-square ($\chi^2$) minimization technique, confirming the robustness of the selected EEC model.

The results indicate that all parameters have acceptable fitting errors, demonstrating that the selected EEC model provides a reliable description of the impedance spectrum [35,43]. Figure 3(e) presents

the chi-square values across all SoCs, demonstrating a consistently low trend. This indicates a high goodness of fit, confirming the strong agreement between the experimental data and the EEC model.

***Table 1.*** *Extracted impedance parameters and fitting errors*

| Parameters | SoC, % | | | | |
|---|---|---|---|---|---|
| | 0 | 20 | 50 | 80 | 100 |
| $R_1$ / Ω | 1.054 | 1.068 | 1.362 | 1.465 | 0.96957 |
| $R_2$ / Ω | 20.96 | 17.55 | 6.133 | 4.378 | 0.67631 |
| $CPE_1$, F $s^{n_1-1}$ | 0.014229 | 0.010462 | 0.012997 | 0.015738 | 0.022461 |
| $n_1$ | 0.79214 | 0.89216 | 0.89024 | 0.89796 | 0.94075 |
| $R_3$ / Ω | 3.222 | 0.21495 | 0.49553 | 0.62346 | 3.887 |
| $CPE_2$, F $s^{n_2-1}$ | 0.027641 | 0.026131 | 0.026333 | 0.035825 | 0.017661 |
| $n_2$ | 1.153 | 0.93429 | 0.84356 | 0.78331 | 1.002 |
| $W$ / Ω $s^{-1/2}$ | 22.32 | 18.44 | 14.34 | 13.17 | 9.044 |
| $\chi^2$ / $10^5$ | 6.80 | 2.27 | 2.32 | 1.84 | 14.48 |
| Sum of squares | 0.001361 | 0.000453 | 0.000465 | 0.000368 | 0.0028953 |

Comparative analysis revealed that $AB_5$ and $A_2B_7$ batteries exhibit optimal performance at full and mid-range SoC, characterized by lower charge transfer resistance and Warburg impedance, enabling efficient ion mobility and electrochemical activity. However, the $A_2B_7$ battery demonstrated slightly superior electrochemical performance overall, particularly at higher SoC levels. At low SoC, both batteries experienced higher resistance and reduced ion mobility, reflected in elevated impedance values. This analysis underscores the importance of understanding electrochemical parameters at varying SoC levels for optimizing battery performance.

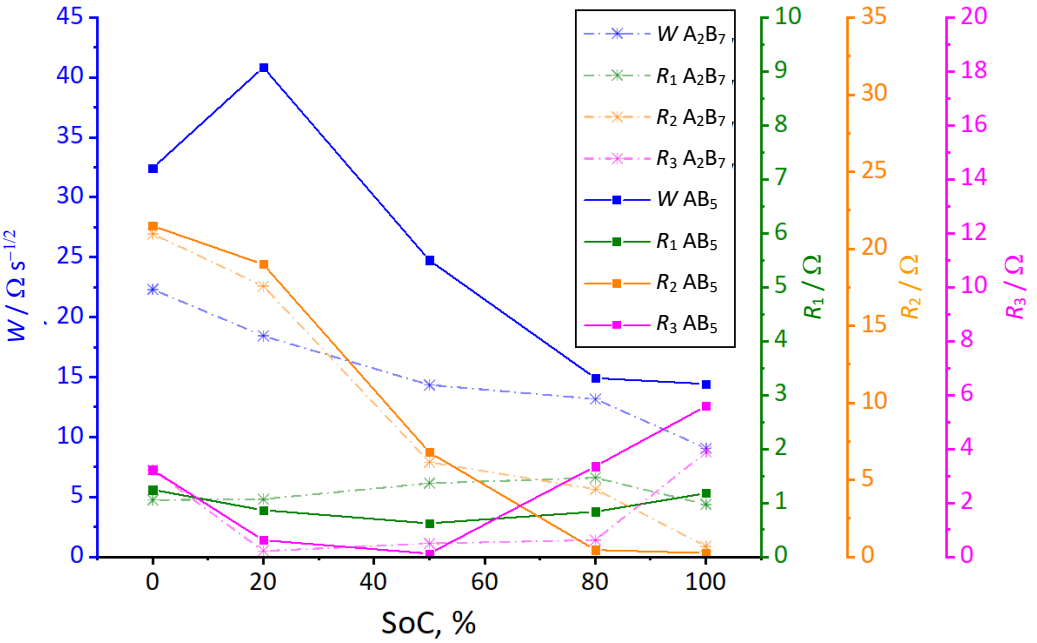


***Figure 4****. Impedance parameter values obtained by fitting of equivalent circuit model shown in Figure 1 to Nyquist plots shown in Figure 3*

*Hydrogen diffusion coefficient*

The diffusion coefficient of hydrogen ($D_H$) quantifies the rate at which hydrogen ions move through a material, typically driven by a concentration gradient. In this study, the determination of $D_H$ is closely linked to the Warburg impedance. For systems involving hydrogen diffusion, such as

electrochemical reactions at an electrode, Warburg impedance characterizes the impact of slow hydrogen ion transport through the medium. This response reflects diffusion-controlled processes influenced by mass transfer limitations, particularly in the low-frequency region of the impedance spectrum [44]. The calculation of $D_H$ incorporates Fick's diffusion law, which provides a simplified approach for evaluating hydrogen diffusion coefficients. The simplified form is presented by Equation (1) [41]:

$$D_H = \frac{R^2T^2}{2A^2n^4F^4C^2\sigma^2} \quad (1)$$

The parameters used in the calculation of the hydrogen diffusion coefficient $D_H$ are defined as follows: $D_H$ represents the hydrogen diffusion coefficient, $R$ is the ideal gas constant, $T$ is the absolute temperature, $A$ denotes the active surface area per unit volume of the electrode, $n$ is the number of electrons transferred ($n$ = 1), $C$ is the hydrogen ion concentration (0.006 mol cm$^{-3}$, as reported in [45]), and σ is the Warburg coefficient in the low-frequency region. The active surface area A is calculated using the following equation [46]:

$$A = \frac{3(1-\varepsilon)}{r} \quad (2)$$

where $\epsilon$ = is the electrode porosity, assumed to be 0.3 [45], and $r$ is the radius of the negative electrode particles, ranging from 2.5 to 5.1 µm.

The calculated $D_H$ values for $AB_5$ and $A_2B_7$ batteries at different SoC levels (0, 20, 50, 80 and 100 %) are shown in Figure 5. Across all SoC levels, the $A_2B_7$ battery consistently exhibits a higher hydrogen diffusion coefficient compared to the $AB_5$ battery. A higher $D_H$ value indicates more efficient and rapid hydrogen diffusion between the positive and the negative electrodes during charging and discharging. Enhanced diffusion facilitates more optimal hydrogen release and storage, improving battery performance [47].

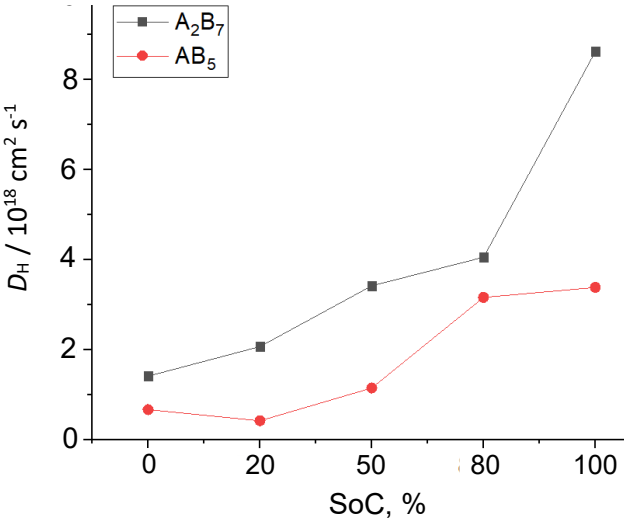


***Figure 5**. Comparison of $D_H$ value of $AB_5$ and $A_2B_7$ batteries*

The calculated diffusion coefficient values range from $10^{-18}$ to $10^{-17}$ cm$^2$ s$^{-1}$, lower than typical literature values for similar electrochemical systems. Several factors may contribute to this discrepancy. First, differences in electrode microstructure, such as grain boundaries, particle morphology, or surface oxidation, can significantly affect hydrogen transport and lead to a lower apparent $D_H$. Second, the experimental conditions, particularly the frequency range used in impedance fitting, could influence the extracted Warburg coefficient and, consequently, the diffusion coefficient. A

narrow low-frequency range may lead to an overestimation of the Warburg impedance and an underestimation of $D_H$. Additionally, surface passivation or hydrogen trapping at defect sites within the electrode material may reduce the effective diffusion rate.

It is also important to note that diffusion coefficients reported in the literature are often derived from different experimental techniques, such as chronoamperometry or electrochemical permeation, which may measure hydrogen transport under different conditions. Therefore, while our values are lower than those reported elsewhere, they remain internally consistent within our experimental framework and provide valuable insights into the diffusion behaviour of hydrogen in these alloy systems.

*Cyclic voltammograms*

In cyclic voltammetry testing, battery samples undergo two stages of potential variation. During the first stage, the potential is increased at a constant scan rate until it reaches a predetermined final value, known as the switching potential. In the second stage, the potential is decreased at the same rate, returning to the initial value. The current response of the battery is recorded as a current-voltage (*I* - *V*) plot, referred to as a cyclic voltammogram, as illustrated in Figure 6.

At the beginning of the cycle, the current increases gradually, a phase identified as the background region in the voltammogram. As the applied potential approaches the electrode's standard potential ($E^0$), a faradaic current is observed, indicating a rapid electrochemical reaction. This results in a sharp rise in current. As the potential continues to increase, the reaction becomes diffusion-limited due to the depletion of ions at the electrode surface, causing the current to decline and form peak currents. These peaks represent the anodic and cathodic reactions occurring during the process [48]. In this study, the cyclic voltammogram characteristics, including anodic and cathodic peak currents and the voltage window, are analysed.

Peak current, defined as the difference between the highest current value and the background current, is illustrated in Figure 6(e). In a cyclic voltammogram, two distinct peak currents are observed: anodic peak current ($I_{p,a}$) and cathodic peak current ($I_{p,c}$), corresponding to the maximum current generated during redox reactions within the battery. A higher peak current indicates enhanced hydrogen absorption capacity by the electrode, driven by the availability of hydrogen ions. Figure 6 compares $I_{p,a}$ and $I_{p,c}$ for $AB_5$ and $A_2B_7$ batteries. The anodic current ($I_{p,a}$) represents the discharge process involving the oxidation of the metal hydride electrode, while the cathodic current ($I_{p,c}$) corresponds to the charging process involving the reduction of the metal hydride. From Figure 6(a), the data shows minimal variation in $I_{p,a}$ with changes in the SoC. The $AB_5$ battery demonstrates a higher $I_{p,a}$ compared to $A_2B_7$, suggesting that $AB_5$ has a greater rate of hydrogen ion release during oxidation reactions. Furthermore, $I_{p,a}$ for $AB_5$ remains relatively stable across varying SoC levels, indicating more efficient hydrogen ion release during oxidation reactions, while $A_2B_7$ displays noticeable fluctuations suggesting enhanced dopant ion capture in the electrolyte near the electrode during reduction reactions. A higher $I_{p,a}$ reflects greater current reaching its maximum at the anodic peak potential, while a higher $I_{p,c}$ indicates increased ion availability for redox reactions at the electrode interface.

For $I_{p,c}$, the data indicate that as SoC increases, $I_{p,c}$ becomes more negative, signifying improved hydrogen ion reduction and captured by the metal hydride at higher SoC levels. This improvement is likely attributed to the greater availability of hydrogen ions in the electrolyte at elevated SoC, facilitating enhanced reaction rates at the electrode surface. Both batteries exhibit comparable performance in $I_{p,c}$, with no significant differences observed between their respective trends.

The voltage window illustrated in Figure 6(h) represents the range between faradaic currents during the oxidation and reduction cycles, reflecting the region where active reactions occur at the battery electrodes.

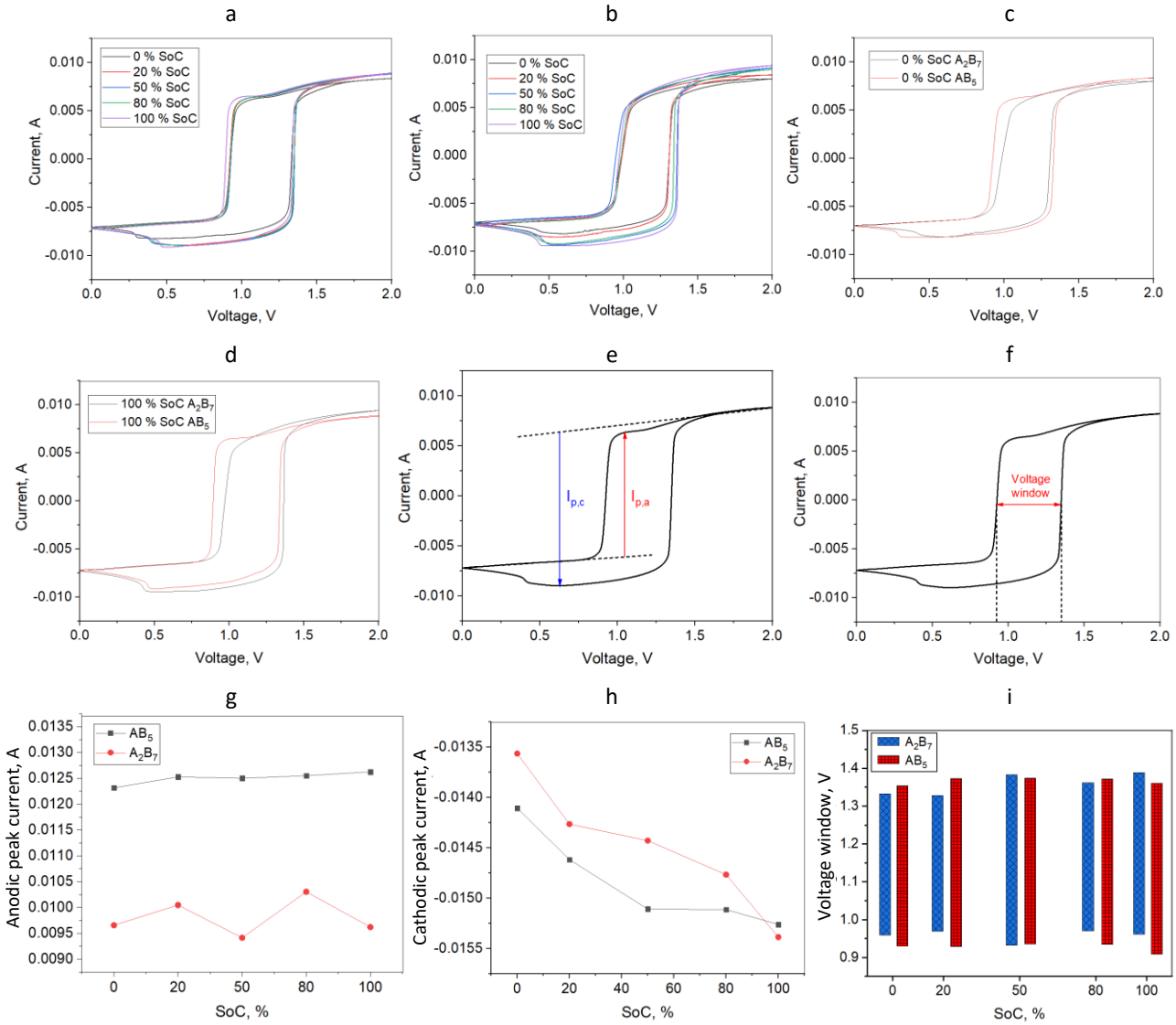


***Figure 6**. Voltammograms of $AB_5$ (a) and $A_2B_7$ (b) batteries across all SoC levels, showcasing distinct shapes that reflect irreversible redox reactions during CV tests. Voltammograms at 0 % SoC (c) and 100 % SoC (d) highlight the evolution of redox reaction characteristics with increasing SoC. Key voltammogram features are visualized in: (e) anodic peak current ($I_{p,a}$) and cathodic peak current ($I_{p,c}$), and (f) voltage window. The plots of $I_{p,a}$ (g) and $I_{p,c}$ (h) versus SoC illustrate the differences in redox behaviour between the two battery types*

A broader voltage window signifies the electrode's ability to facilitate hydrogen ion ($H^+$) absorption and release over a wider voltage range, leading to increased charge and discharge capacities due to the enhanced storage and release of hydrogen ions [49]. Figure 6 compares the voltage windows of the $AB_5$ and the $A_2B_7$ batteries. The $AB_5$ battery exhibits a wider voltage window than the $A_2B_7$ battery, except at 50 % SoC. The widest voltage window for the $AB_5$ battery occurs at 100 % SoC, measuring 0.43945 V, while the $A_2B_7$ battery reaches its maximum voltage window at 50 % SoC, measuring 0.4126 V. Additionally, the $AB_5$ battery demonstrates greater stability in its voltage window across varying SoC levels compared to the $A_2B_7$ battery, indicating superior performance and reliability.

*X-ray diffraction patterns*

X-ray diffraction (XRD) analysis reveals that the diffraction pattern of the $A_2B_7$ battery corresponds to the $Ce_2Ni_7$ compound, whereas the $AB_5$ battery aligns with the $Ce(CoCu)_{2.5}$ compound (see Figure 7). A comparison of diffraction patterns at 0 and 100 % SoC indicates changes in peak intensity, suggesting variations in crystallite size. A higher intensity in the XRD pattern indicates more atoms scattering X-rays in the $A_2B_7$ compared to the $AB_5$ battery, which suggests a higher number of atoms in the crystal, which could indicate a higher degree of crystallinity or larger crystal size [50].

These changes in crystallite size are quantified using the Scherrer Equation (2) [51-53]:

$$\text{Crystallite size} = \frac{k\lambda}{\beta \cos\theta} \quad (2)$$

Table 2 shows the calculation result for the crystallite size of both battery types. Both batteries experience an increase in crystallite diameter from SoC of 0 to 100 %. In the $A_2B_7$ battery, the diameter increased from 35.580 nm to 51.928 nm, while in the $AB_5$ battery, the diameter increased from 25.540 nm to 31.884 nm. This increase can be attributed to the absorption of hydrogen ions by the negative electrode during the battery charging process, causing the electrode grain diameter to grow as the SoC increases [49,50]. Comparing both diameters, the $A_2B_7$ was found to have a slightly bigger crystallite size, which reflects the hydrogen storage capacity, with larger crystallite sizes indicating greater hydrogen storage capability [14]. It was also found that the crystallite diameter in the $A_2B_7$ battery increased by 45.95 %, while in the $AB_5$ battery, it increased by 24.84 %.

***Table 2.*** *Crystallite size calculation result using Scherer formula, Equation (2)*

| Type | SoC, % | Diameter, nm | Crystallite size, nm |
|---|---|---|---|
| $A_2B_7$ | 0 | 35.580 | 16.348 |
| | 100 | 51.928 | |
| $AB_5$ | 0 | 25.540 | 6.344 |
| | 100 | 31.884 | |

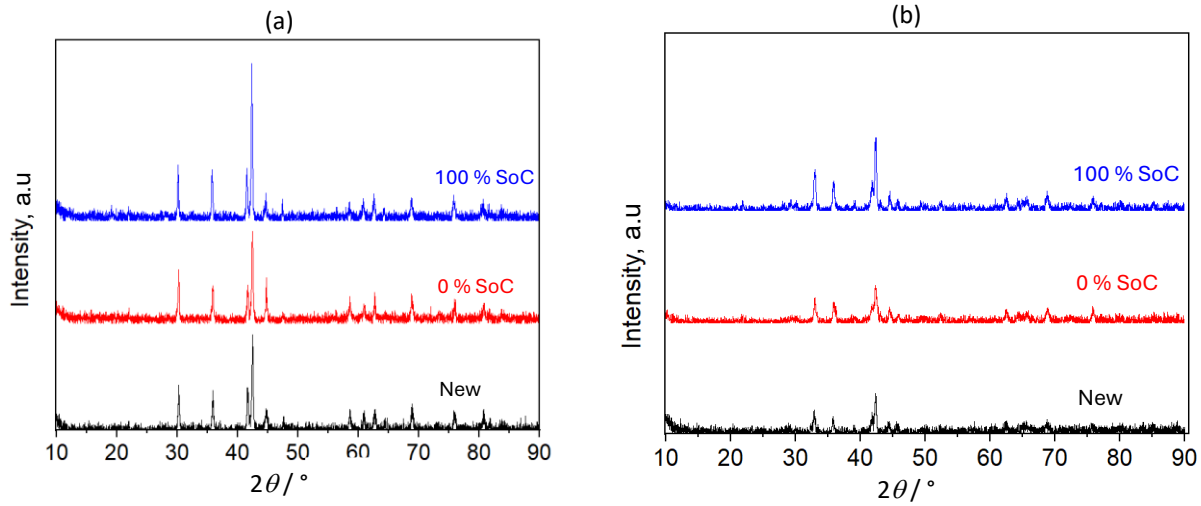


***Figure 7.*** *XRD patterns for $A_2B_7$* ***(a)*** *and $AB_5$* ***(b)*** *for a new battery*

Figure 8 presents SEM images of the negative electrode powders for the $AB_5$ and the $A_2B_7$ metal hydride batteries at 0 and 100 % SoC. Grain size measurements derived from the images indicate no significant difference at 0 % SoC, with diameters (estimation)of 25.35 µm for the $A_2B_7$ battery and 26.83 µm for the $AB_5$ battery. However, at 100 % SoC, a more pronounced difference is observed, with the $A_2B_7$ battery exhibiting a grain diameter (estimation) of 46.53 µm compared to 39.13 µm

for the $AB_5$ battery. The results also show grain diameter increases as the SoC rises from 0 to 100 %. This increase is more pronounced in the $A_2B_7$ battery, which exhibits a 45.51 % growth in grain diameter, compared to a 31.44 % increase in the $AB_5$ battery. This difference highlights the superior hydrogen absorption and storage behaviour of the $A_2B_7$ battery during the charging process [54,55].

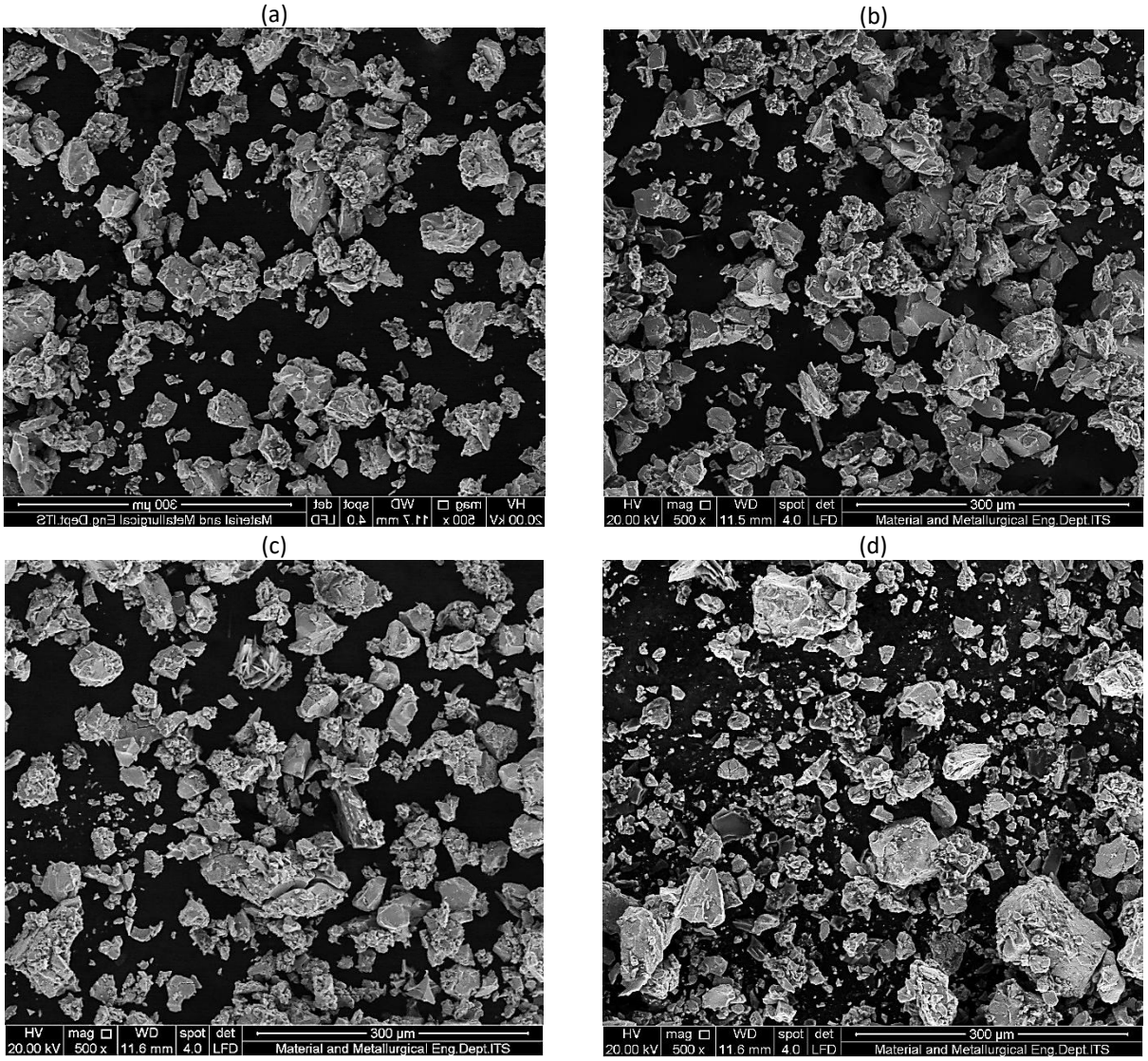


***Figure 8.*** *SEM images of the negative electrode of $AB_5$ battery at 0 (a) and 100 % SoC (b) and $A_2B_7$ battery at 0 (c) and 100 % SoC (d)*

## Conclusions

The effect of the SoC on the performance of NiMH batteries was evaluated using EIS, CV, XRD, and SEM. EIS results demonstrated that the resistances of both $A_2B_7$ and $AB_5$ batteries decreased with increasing SoC, reaching their lowest values at 100 % SoC. $D_H$ calculations revealed that hydrogen diffusion was most effective at 100 % SoC and least effective at 0 % SoC for the $A_2B_7$ battery, while for the $AB_5$ battery, diffusion was optimal at 100 % SoC and poorest at 20 % SoC. These findings align with CV analysis, which showed that the cathodic peak current ($I_{p,c}$) became more negative with increasing SoC, indicating improved hydrogen ion reduction and capture at higher SoC levels. This improvement is attributed to the greater availability of hydrogen ions in the electrolyte, which enhances reaction rates at the electrode surface.

The cyclic voltammogram also revealed that the voltage window, a key indicator of hydrogen storage capacity, widened with increasing SoC. The largest hydrogen storage capacity was observed at 100 % SoC for the $AB_5$ battery and 50 % SoC for the $A_2B_7$ battery, with the $A_2B_7$ battery displaying a notable spike in voltage window width at 50 % SoC. SEM and XRD analyses at 0 and 100 % SoC indicated that both the grain size of the negative electrode particles and the crystallite size increased at higher SoC levels, suggesting enhanced hydrogen storage and a corresponding increase in capacity.

The $A_2B_7$ battery generally exhibited a higher hydrogen diffusion coefficient than the $AB_5$ battery. However, contrary to this trend, the $AB_5$ battery produced higher anodic peak currents ($I_{p,a}$), indicating superior reaction kinetics during discharging. This discrepancy could be influenced by factors such as manufacturing processes and battery morphology. SEM analysis revealed that the $AB_5$ electrode had smaller average particle sizes than the $A_2B_7$ electrode, resulting in a larger surface area for hydrogen transfer. Additionally, although the charge transfer resistance ($R_3$) was lower for the $A_2B_7$ battery, its electrolyte resistance ($R_1$) was slightly higher than that of the $AB_5$ battery. These observations highlight the complex interplay of factors beyond metal hydride type, including electrode morphology and material properties affecting battery discharge performance.

***Acknowledgments:*** *The authors gratefully acknowledge financial support from Institut Teknologi Sepuluh Nopember (ITS) for this work, under project scheme of the Scientific Research Program (Program Penelitian Keilmuan) 2024 no. 1141/PKS/ITS/2024.*

**References**

[1] S. O. Rey, J. A. Romero, L. T. Romero, À. F. Martínez, X. S. Roger, M. A. Qamar, J. L. Domínguez-García, L. Gevorkov, Powering the Future: A Comprehensive Review of Battery Energy Storage Systems, *Energies* **16** (2023) 6344. https://doi.org/10.3390/en16176344

[2] Z. Yi, Z. Chen, K. Yin, L. Wang, K. Wang, Sensing as the key to the safety and sustainability of new energy storage devices, *Protection and Control of Modern Power Systems* **8** (2023) 27. https://doi.org/10.1186/s41601-023-00300-2

[3] S.O. Rey, J.A. Romero, L.T. Romero, À.F. Martínez, X.S. Roger, M.A. Qamar, J.L. Domínguez-García, L. Gevorkov, Powering the Future: A Comprehensive Review of Battery Energy Storage Systems, *Energies* **16** (2023) 6344. https://doi.org/10.3390/en16176344.

[4] A. Saldarini, M. Longo, M. Brenna, D. Zaninelli, Battery Electric Storage Systems: Advances, Challenges, and Market Trends, *Energies* **16** (2023) 7566. https://doi.org/10.3390/en16227566

[5] M. Iqbal, A. Benmouna, M. Becherif, S. Mekhilef, Survey on Battery Technologies and Modeling Methods for Electric Vehicles, *Batteries* **9** (2023) 185. https://doi.org/10.3390/batteries9030185

[6] W. Xie, K. Zhu, H. Yang, W. Yang, Advancements in Achieving High Reversibility of Zinc Anode for Alkaline Zinc-Based Batteries, *Advanced Materials* **36** (2024) 2306154. https://doi.org/10.1002/adma.202306154

[7] R. Martínez-Sánchez, A. Molina-García, A. P. Ramallo-González, Regeneration of Hybrid and Electric Vehicle Batteries: State-of-the-Art Review, Current Challenges, and Future Perspectives, *Batteries* **10** (2024) 101. https://doi.org/10.3390/batteries10030101

[8] Reportlinker, Global Nickel-Metal Hydride (Ni-MH) Battery Market 2018-2022. https://www.prnewswire.com/news-releases/global-nickel-metal-hydride-ni-mh-battery-market-2018-2022-300667854.html (accessed November 2, 2024).

[9] NiMH Battery Industry 2024. https://www.reportlinker.com/market-report/Battery/474883/NiMH-Battery (accessed November 2, 2024).

[10] ReportLinker, Global Battery Market 2023-2027, GlobeNewswire News Room (2022). https://www.globenewswire.com/en/news-release/2022/12/30/2581197/0/en/Global-Battery-Market-2023-2027.html (accessed November 2, 2024).
[11] B. Ash, V. S. Nalajala, A. K. Popuri, T. Subbaiah, M. Minakshi, Perspectives on Nickel Hydroxide Electrodes Suitable for Rechargeable Batteries: Electrolytic vs. Chemical Synthesis Routes, *Nanomaterials* **10** (2020) 1878. https://doi.org/10.3390/nano10091878
[12] M. Patel, K. Mishra, R. Banerjee, J. Chaudhari, D. K. Kanchan, D. Kumar, Fundamentals, recent developments and prospects of lithium and non-lithium electrochemical rechargeable battery systems, *Journal of Energy Chemistry* **81** (2023) 221-259. https://doi.org/10.1016/j.jechem.2023.02.023
[13] L. Ouyang, J. Huang, H. Wang, J. Liu, M. Zhu, Progress of hydrogen storage alloys for Ni-MH rechargeable power batteries in electric vehicles: A review, *Materials Chemistry and Physics* **200** (2017) 164-178. https://doi.org/10.1016/j.matchemphys.2017.07.002
[14] K. Young, S. Yasuoka, Capacity Degradation Mechanisms in Nickel/Metal Hydride Batteries, *Batteries* **2** (2016) 3. https://doi.org/10.3390/batteries2010003
[15] W. H. Zhu, Y. Zhu, B. J. Tatarchuk, Self-discharge characteristics and performance degradation of Ni-MH batteries for storage applications, *International Journal of Hydrogen Energy* **39** (2014) 19789-19798. https://doi.org/10.1016/j.ijhydene.2014.09.113
[16] F. Feng, M. Geng, D. O. Northwood, Electrochemical behaviour of intermetallic-based metal hydrides used in Ni/metal hydride (MH) batteries: a review, *International Journal of Hydrogen Energy* **26** (2001) 725-734. https://doi.org/10.1016/S0360-3199(00)00127-0
[17] Y. Kang, K. Zhang, X. Lin, Surface Modifications of Magnesium-Based Materials for Hydrogen Storage and Nickel-Metal Hydride Batteries: A Review, *Coatings* **13** (2023) 1100. https://doi.org/10.3390/coatings13061100
[18] Y. Xu, F.M. Mulder, Non-alloy Mg anode for Ni-MH batteries: Multiple approaches towards a stable cycling performance, *International Journal of Hydrogen Energy* **46** (2021) 19542-19553. https://doi.org/10.1016/j.ijhydene.2021.03.073
[19] T. Franke, J. F. Krems, Understanding charging behaviour of electric vehicle users, *Transportation Research Part F: Traffic Psychology and Behaviour* **21** (2013) 75-89. https://doi.org/10.1016/j.trf.2013.09.002
[20] S. Geng, Y. Zhang, B. Xie, A. Shi, Y. Ning, S. Lou, G. Yin, Challenges and Opportunities for Fast-Charging Batteries, *The Journal of Physical Chemistry C* **127** (2023) 15021-15034. https://doi.org/10.1021/acs.jpcc.3c01927
[21] S. R. Salkuti, Electrochemical batteries for smart grid applications, *International Journal of Electrical and Computer Engineering (IJECE)* **11** (2021) 1849-1856. http://doi.org/10.11591/ijece.v11i3.pp1849-1856
[22] S. Watanabe, M. Kinoshita, T. Hosokawa, K. Morigaki, K. Nakura, Capacity fade of $LiAl_yNi_{1-x-y}Co_xO_2$ cathode for lithium-ion batteries during accelerated calendar and cycle life tests (surface analysis of $LiAl_yNi_{1-x-y}Co_xO_2$ cathode after cycle tests in restricted depth of discharge ranges), *Journal of Power Sources* **258** (2014) 210-217. https://doi.org/10.1016/j.jpowsour.2014.02.018
[23] J. Kwon, K. Eom, Effects of Oversaturated Cathode Humidity Conditions on the Performance Degradation of PEMFCs and Diagnostic Signals of Warburg Impedance under Low Humidity Conditions, *The Journal of Physical Chemistry C* **125** (2021) 10824-10834. https://doi.org/10.1021/acs.jpcc.1c02805
[24] R. Tiwari, D. Kumar, D. K. Verma, K. Parwati, P. Ranjan, R. Rai, S. Krishnamoorthi, R. Khan, Fundamental chemical and physical properties of electrolytes in energy storage devices: A review, *Journal of Energy Storage* **81** (2024) 110361. https://doi.org/10.1016/j.est.2023.110361

[25] R. Nölle, K. Beltrop, F. Holtstiege, J. Kasnatscheew, T. Placke, M. Winter, A reality check and tutorial on electrochemical characterization of battery cell materials: How to choose the appropriate cell setup, *Materials Today* **32** (2020) 131-146. https://doi.org/10.1016/j.mattod.2019.07.002

[26] S. Cruz-Manzo, P. Greenwood, R. Chen, An Impedance Model for EIS Analysis of Nickel Metal Hydride Batteries, *Journal of The Electrochemical Society* **164** (2017) A1446. https://doi.org/10.1149/2.0431707jes

[27] I. D. Wijayanti, V. A. Yartys, Studies of the effect of Hf doping on the electrochemical performance of C15 Laves type metal hydride battery anode alloys, *Journal of Energy Storage* **60** (2023) 106627. https://doi.org/10.1016/j.est.2023.106627

[28] I. D. Wijayanti, R. Denys, Suwarno, A. A. Volodin, M. V. Lototskyy, M. N. Guzik, J. Nei, K. Young, H. J. Roven, V. Yartys, Hydrides of Laves type Ti-Zr alloys with enhanced H storage capacity as advanced metal hydride battery anodes, *Journal of Alloys and Compounds* **828** (2020) 154354. https://doi.org/10.1016/j.jallcom.2020.154354

[29] D. Zhu, W. Zhou, Z. Tang, Y. Heng, K. Liu, J. Li, L. Xie, Y. Chen, SOC-dependent high-rate dischargeability of $AB_5$-type metal hydride anode: Mechanism linking phase transition to electrochemical H-desorption kinetics, *International Journal of Hydrogen Energy* **44** (2019) 15278-15286. https://doi.org/10.1016/j.ijhydene.2019.04.078

[30] Q. Li, D. Yi, G. Dang, H. Zhao, T. Lu, Q. Wang, C. Lai, J. Xie, Electrochemical Impedance Spectrum (EIS) Variation of Lithium-Ion Batteries Due to Resting Times in the Charging Processes, *World Electric Vehicle Journal* **14** (2023) 321. https://doi.org/10.3390/wevj14120321

[31] T. Osaka, T. Momma, D. Mukoyama, H. Nara, Proposal of novel equivalent circuit for electrochemical impedance analysis of commercially available lithium ion battery, *Journal of Power Sources* **205** (2012) 483-486. https://doi.org/10.1016/j.jpowsour.2012.01.070

[32] R. Alicki, D. Gelbwaser-Klimovsky, A. Jenkins, E. von Hauff, Dynamical theory for the battery's electromotive force, *Physical Chemistry Chemical Physics* **23** (2021) 9428-9439. https://doi.org/10.1039/D1CP00196E

[33] F. Huet, A review of impedance measurements for determination of the state-of-charge or state-of-health of secondary batteries, *Journal of Power Sources* **70** (1998) 59-69. https://doi.org/10.1016/S0378-7753(97)02665-7

[34] E. Karden, S. Buller, R. W. De Doncker, A method for measurement and interpretation of impedance spectra for industrial batteries, *Journal of Power Sources* **85** (2000) 72-78. https://doi.org/10.1016/S0378-7753(99)00385-7

[35] J. Yang, Y. Xia, Enhancement on the Cycling Stability of the Layered Ni-Rich Oxide Cathode by In-Situ Fabricating Nano-Thickness Cation-Mixing Layers, *Journal of The Electrochemical Society* **163** (2016) A2665. https://doi.org/10.1149/2.0841613jes

[36] M. Tliha, C. Khaldi, J. Lamloumi, AC Impedance Behavior of $LaNi_{3.55}Mn_{0.4}Al_{0.3}Co_{0.6}Fe_{0.15}$ Hydrogen-Storage Alloy: Effect of Surface Area, *Journal of Materials Engineering and Performance* **25** (2016) 1578-1585. https://doi.org/10.1007/s11665-016-1980-0

[37] T. F. Landinger, G. Schwarzberger, A. Jossen, High frequency impedance characteristics of cylindrical lithium-ion cells: Physical-based modeling of cell state and cell design dependencies, *Journal of Power Sources* **488** (2021) 229463. https://doi.org/10.1016/j.jpowsour.2021.229463

[38] X. Zhou, K. Young, J. West, J. Regalado, K. Cherisol, Degradation mechanisms of high-energy bipolar nickel metal hydride battery with AB5 and A2B7 alloys, *Journal of Alloys and Compounds* **580** (2013) S373-S377. https://doi.org/10.1016/j.jallcom.2013.03.014

[39] N. Kuriyama, T. Sakai, H. Miyamura, I. Uehara, H. Ishikawa, T. Iwasaki, Electrochemical impedance and deterioration behavior of metal hydride electrodes, J*ournal of Alloys and Compounds* **202** (1993) 183-197. https://doi.org/10.1016/0925-8388(93)90538-X

[40] I. D. Wijayanti, L. Mølmen, R. V. Denys, J. Nei, S. Gorsse, M. N. Guzik, K. Young, V. Yartys, Studies of Zr-based C15 type metal hydride battery anode alloys prepared by rapid solidification, *Journal of Alloys and Compounds* **804** (2019) 527-537. https://doi.org/10.1016/j.jallcom.2019.06.324

[41] A. A. Volodin, R. V. Denys, C. Wan, I. D. Wijayanti, Suwarno, B. P. Tarasov, V.E . Antonov, V. A. Yartys, Study of hydrogen storage and electrochemical properties of $AB_2$-type $Ti_{0.15}Zr_{0.85}La_{0.03}Ni_{1.2}Mn_{0.7}V_{0.12}Fe_{0.12}$ alloy, *Journal of Alloys and Compounds* **793** (2019) 564-575. https://doi.org/10.1016/j.jallcom.2019.03.134

[42] N. Küçükdeveci, I. Akay Erdoğan, A. Binal Aybar, Effects of Zr addition on electrochemical characteristics of MgTiMnNi hydrogen storage alloys, *International Journal of Hydrogen Energy* **48** (2023) 18753-18760. https://doi.org/10.1016/j.ijhydene.2023.01.307

[43] S. Effendy, J. Song, M. Z. Bazant, Analysis, Design, and Generalization of Electrochemical Impedance Spectroscopy (EIS) Inversion Algorithms, *Journal of The Electrochemical Society* **167** (2020) 106508. https://doi.org/10.1149/1945-7111/ab9c82

[44] W. Lai, S. M. Haile, Impedance Spectroscopy as a Tool for Chemical and Electrochemical Analysis of Mixed Conductors: A Case Study of Ceria, *Journal of the American Ceramic Society* **88** (2005) 2979-2997. https://doi.org/10.1111/j.1551-2916.2005.00740.x

[45] P. D. Vidts, J. Delgado, R. E. White, Mathematical Modeling for the Discharge of a Metal Hydride Electrode, *Journal of The Electrochemical Society* **142** (1995) 4006. https://doi.org/10.1149/1.2048454

[46] S. Malifarge, B. Delobel, C. Delacourt, Determination of Tortuosity Using Impedance Spectra Analysis of Symmetric Cell, *Journal of The Electrochemical Society* **164** (2017) E3329. https://doi.org/10.1149/2.0331711jes

[47] A. M. Svensson, L. O. Valøen, R. Tunold, Modeling of the impedance response of porous metal hydride electrodes, *Electrochimica Acta* **50** (2005) 2647-2653. https://doi.org/10.1016/j.electacta.2004.11.035

[48] N. Elgrishi, K. J. Rountree, B. D. McCarthy, E. S. Rountree, T. T. Eisenhart, J. L. Dempsey, A Practical Beginner's Guide to Cyclic Voltammetry, *Journal of Chemical Education* **95** (2018) 197-206. https://doi.org/10.1021/acs.jchemed.7b00361

[49] C. Iwakura, S. Nohara, N. Furukawa, H. Inoue, The possible use of polymer gel electrolytes in nickel/metal hydride battery, *Solid State Ionics* **148** (2002) 487-492. https://doi.org/10.1016/S0167-2738(02)00092-9

[50] N. M. Deraz, Size and crystallinity-dependent magnetic properties of copper ferrite nano-particles, *Journal of Alloys and Compounds* **501** (2010) 317-325. https://doi.org/10.1016/j.jallcom.2010.04.096

[51] F. T. L. Muniz, M. A. R. Miranda, C. Morilla dos Santos, J. M. Sasaki, The Scherrer equation and the dynamical theory of X-ray diffraction, *Acta Crystallographica Section A: Foundations and Advances* **72** (2016) 385-390. https://doi.org/10.1107/S205327331600365X

[52] S. Sleiman, J. Huot, Effect of particle size, pressure and temperature on the activation process of hydrogen absorption in TiVZrHfNb high entropy alloy, *Journal of Alloys and Compounds* **861** (2021) 158615. https://doi.org/10.1016/j.jallcom.2021.158615

[53] L. J. Huang, H. Wang, L. Z. Ouyang, D. L. Sun, H. J. Lin, M. Zhu, Achieving fast hydrogenation by hydrogen-induced phase separation in Mg-based amorphous alloys, *Journal of Alloys and Compounds* **887** (2021) 161476. https://doi.org/10.1016/j.jallcom.2021.161476

[54] M. Geng, J. Han, F. Feng, D.O. Northwood, Hydrogen-absorbing alloys for the NICKEL-METAL hydride battery, *International Journal of Hydrogen Energy* **23** (1998) 1055-1060. https://doi.org/10.1016/S0360-3199(98)00020-2

[55] N. Küçükdeveci, I. Akay Erdoğan, A. Binal Aybar, M. Anik, Electrochemical hydrogen storage properties of mechanically alloyed $Mg_{0.8}Ti_{0.2-x}Mn_xNi$ (x = 0, 0.025, 0.05, 0.1) type alloys, *International Journal of Hydrogen Energy* **47** (2022) 2511-2519. https://doi.org/10.1016/j.ijhydene.2021.10.174